High resolution image reconstruction method for a double-plane PET system with changeable spacing*

Xiao-Yue Gu(顾笑悦)[1,2;1)] Wei Zhou(周魏)[1,2] Lin Li(李琳)[1,2] Long Wei(魏龙)[1,2] Peng-Fei Yin(尹鹏飞)[1,2]
Lei-Min Shang(尚雷敏)[1,2] Ming-Kai Yun(贠明凯)[1,2] Zhen-Rui Lu(卢贞瑞)[1,2] Xian-Chao Huang(黄先超)[1,2]

[1] Key Laboratory of Nuclear Radiation and Nuclear Energy Technology, Institute of High Energy Physics, Chinese Academy of Sciences，Beijing 100049, China
[2] Beijing Engineering Research Center of Radiographic Techniques and Equipment, Beijing 100049, China

Abstract: Breast-dedicated positron emission tomography (PET) imaging techniques have been developed in recent years. Their capacities to detect millimeter-sized breast tumors have been the subject of many studies. Some of them have been confirmed with good results in clinical applications. With regard to biopsy application, a double-plane detector arrangement is practicable, as it offers the convenience of breast immobilization. However, the serious blurring effect of the double-plane PET, with changeable spacing for different breast sizes, should be studied. We investigated a high resolution reconstruction method applicable for a double-plane PET. The distance between the detector planes is changeable. Geometric and blurring components were calculated in real-time for different detector distances, and accurate geometric sensitivity was obtained with a new tube area model. Resolution recovery was achieved by estimating blurring effects derived from simulated single gamma response information. The results showed that the new geometric modeling gave a more finite and smooth sensitivity weight in the double-plane PET. The blurring component yielded contrast recovery levels that could not be reached without blurring modeling, and improved visual recovery of the smallest spheres and better delineation of the structures in the reconstructed images were achieved with the blurring component. Statistical noise had lower variance at the voxel level with blurring modeling at matched resolution, compared to without blurring modeling. In distance-changeable double-plane PET, finite resolution modeling during reconstruction achieved resolution recovery, without noise amplification.

Keywords: breast PET, double-plane PET, reconstruction

PACS: 87.57.nf, 87.57.rh, 87.57.U-, 87.57.uk **DOI:** 10.1088/1674-1137/40/5/058201

1 Introduction

Breast-dedicated positron emission tomography (PET) imaging techniques have been developed in recent years. Their capacities to detect millimeter-sized breast tumors have been the subject of many studies [1−9]. It has been shown that some of these systems are clinically feasible and valuable in the detection of breast tumors [8−11], and majority of them show better spatial resolution performance than whole-body PET.

The two main recent developments in breast-dedicated PET are ring and plane detector arrangements. In considering biopsy applications, a double-plane detector design is more practical than a ring detector because the plane PET is convenient for breast immobilization. Besides, a double-plane system could achieve greater sensitivity with small spacing covering a large solid angle. However, the parallax errors could be serious with a small plane spacing. The penetration effect of the 511 keV photons into the crystals is severer when a photon is incident on the detector with a larger oblique angle into the crystal faces [12]. The effect will lead to deterioration in resolution, as well as offset the advantages gained in sensitivity.

Some hardware approaches have been proposed to compensate for the parallax errors, which could provide depth-of-interaction information [13−15]. However, the complexity of detector design, the accuracy of measurements, and the cost require further investigation. Another approach to compensate the parallax error is to establish an accurate system response matrix in reconstruction [12, 16, 17]. Usually, the improvement in the quality of reconstructed images depends on the accuracy of the resolution model (RM) [18, 19]. In general, the geometric component and detection physics effects information, or blurring factor, of the system matrix should

Received 27 July 2015
∗ Supported by Knowledge Innovation Project of The Chinese Academy of Sciences (KJCX2-EW-N06)
1) E-mail: guxiaoyue@ihep.ac.cn

be well investigated in the resolution model.

The geometric elements of the system matrix can be calculated by using a simple line integral model [20]. More complex models take line-of response (LOR) as a tube [19, 21, 22], or are based on a solid angle [23]. To achieve feasible reconstruction times, pre-calculation and storage of the system matrix are always required in these cases, commonly with geometrical symmetries used. In addition, improvement in spatial resolution can be achieved by modeling detector blurring effects, including crystal penetration, inter-crystal scattering, and crystal misidentification [18, 24−26].

The positron emission mammography (PEM) Flex Solo Scanner, produced by Naviscan Inc., was the first commercial machine with a double-plane PET arrangement. The 6 cm × 16.4 cm detectors are positioned in an opposing fashion and can move to cover the entire 24 cm × 16.4 cm field of view (FOV) [5]. Naviscan did not report the correction method of parallax errors. Note that the changeable distance for different breast sizes makes this effect more difficult to address. Chien-Min Kao studied a reconstruction method for the double-plane detector, and achieved resolution recovery, as well as a drastic reduction of the system response matrix [12]. However, the simulation studied is applicable for a system with static plane spacing. When the distance changes, the system response matrix (SRM) simulation should be repeated for the new detector spacing. Therefore, this method is not suitable for the breast imaging application.

The demand for a new reconstruction method with RM was motivated by the need for the design of the spacing-changeable double-plane PET. With a compact geometry and resolution model reconstruction method, a high resolution and sensitivity performance could be achieved. The final aim is to perform breast biopsy under PET image guidance. We focused our method on the geometric component and the blurring effect in the double-plane PET. The RM method is a combination of Monte Carlo simulation and calculation solution.

2 Materials and methods

2.1 Reconstruction for double-plane PET

We present a new RM method for resolution recovery in the double-plane PET. The system has two opposing detector heads. The distance is changeable between PET planes for different breast sizes, see Fig. 1. The figure also shows the orientations of the cross-plane (blue) and in-plane (red) directions. In general, statistical reconstruction methods are applied, and resolution modeling is carried out in projection space with a three-dimensional (3D) expectation-maximization algorithm.

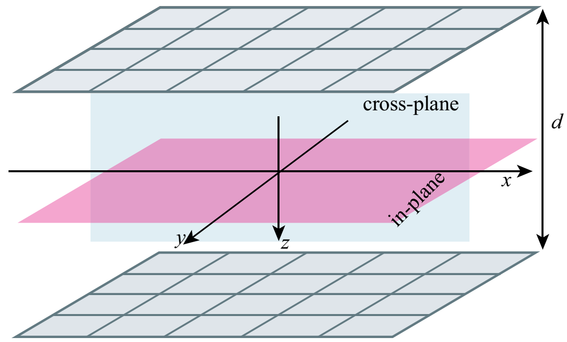

Fig. 1. (color online) The double-plane PET has two opposing detector heads. The distance, d, between the planes is changeable for different breast sizes. The orientations of the in-plane and cross-plane directions are shown.

The system model is of vital importance to any implementation of an iterative reconstruction algorithm. We denote the system matrix as $\boldsymbol{P}\in\boldsymbol{R}^{J\times I}$, the elements of which, $\boldsymbol{p}_{ij}$, model the probability that an event generated in a voxel $j(j=1\cdots J)$ is detected along a tube-of response (TOR) $i(i=1\cdots I)$ [24]. The system matrix is factorized as follows:

$$\boldsymbol{P}=\boldsymbol{P}_{\text{det.sens}}\boldsymbol{P}_{\text{det.blur}}\boldsymbol{P}_{\text{attn}}\boldsymbol{P}_{\text{geom}}\boldsymbol{P}_{\text{positron}}. \quad (1)$$

Here, $\boldsymbol{P}_{\text{attn}}\in\boldsymbol{R}^{I\times I}$ is a diagonal matrix containing the attenuation factors. We applied a calculated attenuation correction method based on breast image segmentation. Attenuation factors was obtained from re-projection of the estimated attenuation map [27]. The diagonal detector normalization matrix $\boldsymbol{P}_{\text{det.sens}}\in\boldsymbol{R}^{I\times I}$ is taken as uniform for the simulated data generated from identical crystals. In addition, we simplified the model with the ^{18}F application and focused on effects other than the positron range effect $\boldsymbol{P}_{\text{positron}}$.

In traditional PET systems, the element number of the system matrix $\boldsymbol{P}$ is always a constant. However, the changeable distance property means that the size of the image space is variable in double-plane PET. With a fixed voxel size, the voxel number $\boldsymbol{J}$ would change with the space detected. The $\boldsymbol{P}_{\text{det.blur}}$ and $\boldsymbol{P}_{\text{geom}}$ factors are related to the size of the image space. Therefore, the two components should be calculated in real time for every scan. With this new attribute, we focus on the two components in our model.

2.1.1 The geometric projection matrix

$\boldsymbol{P}_{\text{geom}}\in\boldsymbol{R}^{J\times I}$ is a matrix that contains the geometric mapping between the source and sino data. Each element (i,j) of $\boldsymbol{P}_{\text{geom}}\in\boldsymbol{R}^{J\times I}$ represents the probability that a photon pair produced in voxel j reaches the front faces of the detector pair i. The tube model is taken to estimate the intersection joining the detector pair with each voxel. The intersection area is used to estimate the normed finite geometric weight.

The image coordinate is defined as Cartesian (x,y,z). When the double planes are exactly parallel, the middle plane of the voxel section is parallel with the in-plane direction. Figure 2 illustrates the relationship between a voxel and tube in double-plane PET. Note that the upper detector face u and the lower detector face l are parallel with the intersection area c. The intersection area c with the tube is always a rectangle for every element (i,j) of $\boldsymbol{P}_{\rm geom}$, see Fig. 3(a). The weight value of element (i,j) can be parameterized by the area $a(i,j)$ of rectangle c, over which the area value is easily calculated in a parallel plane PET by defining the four side boundaries of the rectangle. Formulas (2)-(6) illustrate the boundary calculation method.

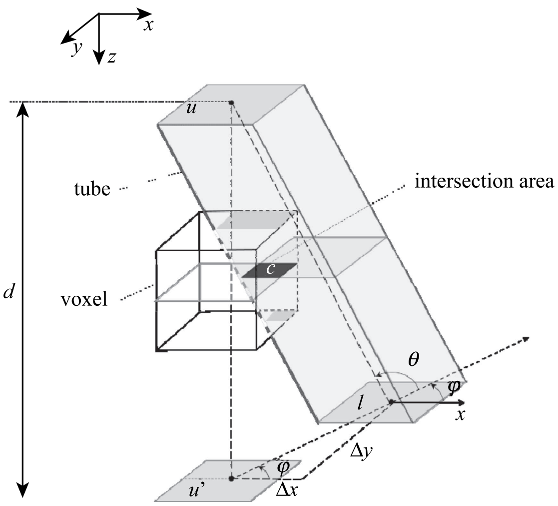

Fig. 2. (color online) The relationship between a voxel and a tube. The tube connects detector element u (upper plane) and detector element l (lower plane). The detector face u' is the projection of u in lower plane. The intersection c (marked as dark gray) is the area of the tube and the center plane of the voxel.

$$a(i,j)=(L_{\rm right}(i,j)-L_{\rm left}(i,j))\times(L_{\rm down}(i,j)-L_{\rm top}(i,j)). \tag{2}$$

$$L_{\rm left}(i,j)=\max(x_{\rm voxel,left}(i,j),x_{\rm tube,left}(i,j)). \tag{3}$$

$$L_{\rm right}(i,j)=\min(x_{\rm voxel,right}(i,j),x_{\rm tube,right}(i,j)). \tag{4}$$

$$L_{\rm top}(i,j)=\max(y_{\rm voxel,top}(i,j),y_{\rm tube,top}(i,j)). \tag{5}$$

$$L_{\rm down}(i,j)=\min(y_{\rm voxel,down}(i,j),y_{\rm tube,down}(i,j)). \tag{6}$$

The factor $a(i,j)$ is the area value of the intersection area c. $L_{\rm left}(i,j)$, $L_{\rm right}(i,j)$, $L_{\rm top}(i,j)$, and $L_{\rm down}(i,j)$ respectively represent the four side boundaries of area c, which are all obtained by comparing the corresponding boundaries of voxel and tube in the in-plane, as shown in Fig. 3. For example, the left boundary $L_{\rm left}(i,j)$ in formula (3) is the larger x value between the left boundaries of the voxel and the tube.

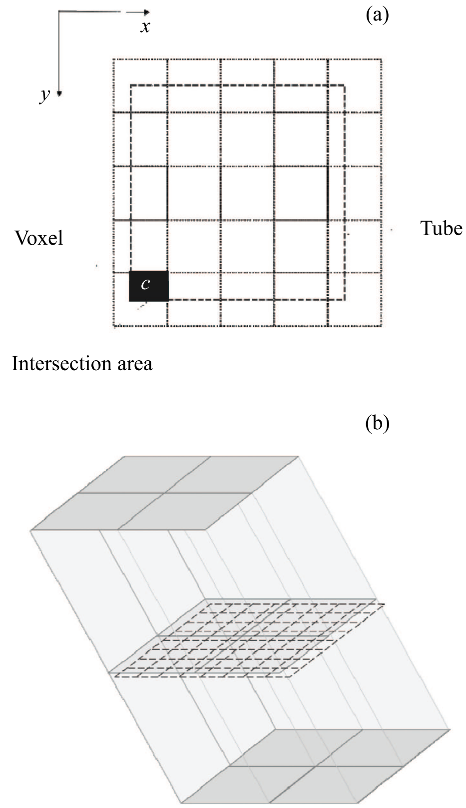

Fig. 3. (a) The finite weight model. (b) The intersection area of voxels and tubes.

Suppose that the detector element is 2 mm × 2 mm and the image voxel is 0.5 mm × 0.5 mm in the in-plane, the length of the tube side would be four times that of the voxel, as illustrated in Fig. 3(b). We take the normed intersection area as the finite weight of the value of the $\boldsymbol{P}_{\rm geom}$ element. In the parallel double-plane system, the intersection area is an approximation of the intersection volume of the tube and the voxel.

2.1.2 The sinogram blurring matrix

$\boldsymbol{P}_{\rm det,blur}$ means the sinogram blurring matrix used to model the photon inter-crystal penetration and inter-crystal scatter effect. Crystals were treated as identical, therefore effects associated with the location within each block were ignored. In principle, the non-collinearity of the photon pair should be accounted for. We therefore simplified the model and focused on the inter-crystal penetration and scatter effects. We did not include subject scattering or positron range in the simulation work.

The detector planes are parallel to the in-plane, located at positions $z=\pm d/2$ (see Fig. 1). We note that double-plane PET projection data are described as $(\boldsymbol{C}_{u_0},\boldsymbol{C}_{l_0})$. $\boldsymbol{C}_{u_0}$ and $\boldsymbol{C}_{l_0}$ denote the indented crystal element in the upper and lower detection planes, respectively. We assume $\boldsymbol{P}_{\rm det,blur}$ equals a five-dimensional coincidence response function (CRF)

$(\boldsymbol{C}_{u_0},\boldsymbol{C}_{l_0},d;\boldsymbol{C}_{u_t},\boldsymbol{C}_{l_t})$. The function maps a given LOR_0 $(\boldsymbol{C}_{u_0},\boldsymbol{C}_{l_0})$ to its blurred counterpart LOR_t $(\boldsymbol{C}_{u_t},\boldsymbol{C}_{l_t})$ with a given distance d between the planes.

We defined the two directions of the detector tube as the oblique angle φ and the azimuthal angle θ. Note that $(\boldsymbol{C}_{u_0},\boldsymbol{C}_{l_0},d;\boldsymbol{C}_{u_t},\boldsymbol{C}_{l_t})$ could also be expressed as $(\boldsymbol{C}_{u_0},\boldsymbol{C}_{l_0},\varphi,\theta;\boldsymbol{C}_{u_t},\boldsymbol{C}_{l_t})$. With a given d value and the incident $LOR_0(\boldsymbol{C}_{u_0},\boldsymbol{C}_{l_0})$, the rotation angle φ and azimuthal angle could be determined as in formula (9). Δy and Δx describe the span in the y and x directions of u and l in the in-plane (see Fig. 2).

$$CRF(\boldsymbol{C}_{u_0},\boldsymbol{C}_{l_0},d;\boldsymbol{C}_{u_t},\boldsymbol{C}_{l_t})$$

$$=CRF(\boldsymbol{C}_{u_0},\boldsymbol{C}_{l_0},\varphi,\theta;\boldsymbol{C}_{u_t},\boldsymbol{C}_{l_t}), \tag{7}$$

$$\varphi=\tan^{-1}(\Delta y/\Delta x), 0\leqslant\varphi\leqslant\pi, \tag{8}$$

$$\theta=\tan^{-1}(-d/2\sqrt{\Delta x^2+\Delta y^2+d^2}), 0\leqslant\theta\leqslant\pi. \tag{9}$$

The distance of source-voxel to detector has an effect in the presence of axial mashing (spanning) in a ring detector [18, 25, 28]. Nevertheless, the manner in which the source-voxel distance affects the distribution of penetration in double-plane PET must be studied. A back-to-back gamma ray source at different distance positions relative to the detector face was simulated with a specified incidence angle ($\varphi=0°, \theta=45°$), as illustrated in Fig. 4(a). The detector spacing was 2 cm, and the source voxel position ranged from the center to the surface of the lower detector plane, with a step of 1 mm, along the TOR direction. The coincidence response of crystal u_0 with each crystal element of the below detector was studied, and denoted as crystal l_0, l_1, l_2 etc. In addition, the profile of the response $LOR_0(\boldsymbol{C}_{u_0},\boldsymbol{C}_{l_0})$ with its main blurred counterparts in the lower plane $LOR_i(\boldsymbol{C}_{u_t},\boldsymbol{C}_{l_t})$ was plotted, as shown in Fig. 4(b). The profile illustrates that different source positions turn as consistent response distribution, and the distribution of the blurring response is independent of the source position in a double-plane PET.

On the basis of the above result, we assumed that the response of gamma ray blurring effects in the plane PET was independent of the source position, and primarily affected by the incidence angle direction into the crystal. In our current implementation, we approximated the blurring effects as the probability product of two separate single gamma ray penetration effects. In summary, the general blurring function was expressed as a coincidence response function (CRF) $(\boldsymbol{C}_{u_0},\boldsymbol{C}_{l_0},\varphi,\theta;\boldsymbol{C}_{u_t},\boldsymbol{C}_{l_t})$, which can be described as follows.

$$CRF(\boldsymbol{C}_{u_0},\boldsymbol{C}_{l_0},\varphi,\theta;\boldsymbol{C}_{u_t},\boldsymbol{C}_{l_t})$$

$$=SGR_u(\boldsymbol{C}_{u_0},\boldsymbol{C}_{u_t},\varphi,\theta)\times SGR_l(\boldsymbol{C}_{l_0},\boldsymbol{C}_{l_t},\varphi,\theta). \tag{10}$$

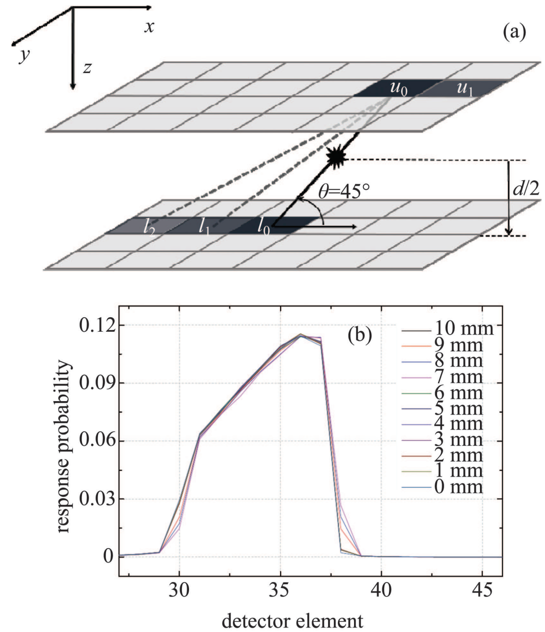

Fig. 4. (color online) Back-to-back gamma ray source with different distances to the detector were simulated at a certain incidence angle (φ=0°, and φ angle direction along with x axis, θ=45°). (a) The tested TORs in the double-plane PET. (b) Response probability results.

The single gamma response $SGR(\boldsymbol{C}_{u_0},\boldsymbol{C}_{u_t},\varphi,\theta)$ function represents the crystal u_0 response probability when the gamma ray incidence to crystal u_i, with an oblique angle of φ and azimuthal angle of θ. With the shift-invariance of double-plane, we focus on the vector $\boldsymbol{u_0u_t}$ and $\boldsymbol{l_0l_t}$. Note that there is origin symmetry between SGR_u and SGR_t functions, and the lower function results could be easily obtained from the upper one.

The SGR was modeled along 2D crystal arrays with different incidence angles. In addition, the SGR simulation could be effectively reduced in consideration of the plane system symmetry of angle φ. The symmetry is as follows:

$$SGR(\boldsymbol{C}_u,\boldsymbol{C}_{u'_0},\varphi,\theta)=SGR(\boldsymbol{C}_u,\boldsymbol{C}_{u'_1},90°+\varphi,\theta),$$
$$u'_0(x,y)=u'_1(y,-x), \tag{11}$$

$$SGR(\boldsymbol{C}_u,\boldsymbol{C}_{u'_0},\varphi,\theta)=SGR(\boldsymbol{C}_u,\boldsymbol{C}_{u'_2},180°+\varphi,\theta),$$
$$u'_0(x,y)=u'_2(-x,-y), \tag{12}$$

$$SGR(\boldsymbol{C}_u,\boldsymbol{C}_{u'_0},\varphi,\theta)=SGR(\boldsymbol{C}_u,\boldsymbol{C}_{u'_3},270°+\varphi,\theta),$$
$$u'_0(x,y)=u'_3(-y,x). \tag{13}$$

With the reduction, the simulation of SRF was effectively reduced to 1/4, with angle φ ranging from 0 to 90 degrees.

The simulation was developed on the basis of the work of Xin [29], and extended into the 3D implementation. The single photon incidence response was obtained with Monte Carlo simulation, and the Geant4 method for emission tomography software was used. A 2D crystal array with 33 × 33 crystal elements was created, as shown in Fig. 5 (only 5 × 5 elements are illustrated). The simulated crystal size was 1.9 mm × 1.9 mm × 10 mm, with a 0.1 mm gap filled with polyvinyl chloride (PVC), which is the same set as in the double-plane PET. The simulation was performed by rotating the single detector along the x and y axles with two directions, θ and φ. The incident single gamma ray was sent into the center crystal u_0. The two directions both ranged from 0 to 90 degrees, with all the incidence angles spanned for different plane distances. There were a total of 18 × 18 (324) directions to simulate with a 5-degree step.

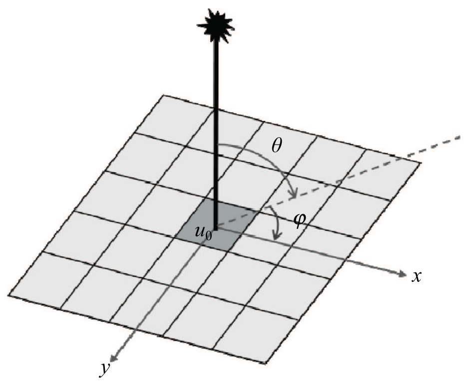

Fig. 5. Single gamma response simulation.

The simulated single gamma ray response results of three incidence angles are shown in Fig. 6. Plots from (a) to (c) illustrate the signal gamma response at 30, 45, and 60 degrees, respectively. The response result turns a distribution of the event counts collected within the crystals. In most conditions, the reaction happened in the gamma ray trajectory, while most crystals outside the trajectory obtained few events. The final blurring factor was calculated on the basis of a single gamma ray response using the formula (11). The simulated SGR is discrete within a 5-degree range, and the particular SGR with an identified incidence angle was calculated from the simulated SGR by linear interpolation.

The accuracy of the calculated CRF derived from the SGR was tested. Three incidence angles were chosen to compare the real CRF with the calculated CRF results, and the calculated value was derived from the product of $SGR_u(\boldsymbol{C}_{u_0},\boldsymbol{C}_{u_t},\varphi,\theta)\times SGR_l(\boldsymbol{C}_{l0},\boldsymbol{C}_{l_t},\varphi,\theta)$. The real CRF was simulated and obtained with the Monte Carlo method, and the incidence angles were chosen as $\varphi=0°,\theta=30°,45°,60°$ for convenient simulation. Figure 7 shows a comparison of the results obtained with the real and calculated CRF. The crystal chosen and data selection are similar to that in the source position study. The profile showed that the calculated CRF (upper profile) was a good approximation to the real CRF (lower profile).

2.2 Double-plane PET data representation

Traditionally, whole-body PET with a ring detector always gives the measured data in (r,ϕ) sinogram mode. The matrix is arranged such that each row represents parallel line integrals or a projection of the activity at a particular angle ϕ. Each column represents the radial offset from the center of the scanner, r [30]. However, in a double-plane PET, the bin number for each acquisition angle ϕ is not a constant. A more oblique angle ϕ covers fewer bin numbers in r. The (r,ϕ) sinogram mode is not applicable for double-plane PET data organization.

The new data structure is collected with crystals in upper detector one by one. The projection data are sorted in a four-dimension al function (x_{upper}, $y_{\text{upper}},x_{\text{lower}},y_{\text{lower}}$). They represent the x and y index of the upper and lower crystals respectively. This result is organized in a 100×75×100×75 array. The image slices of the projection data are shown in Fig. 8. Although the data representation is different from a ring PET, the sinogram data are still taken as projection data in this study.

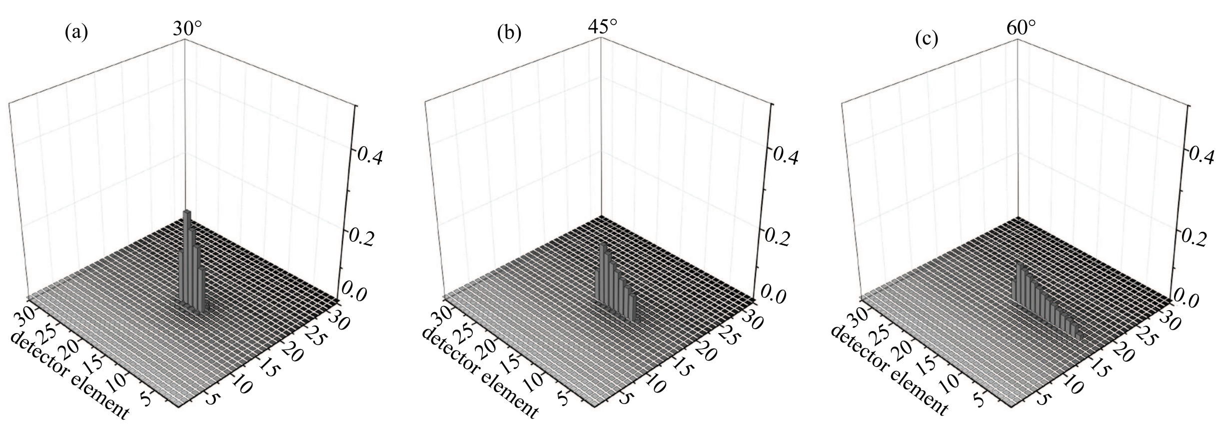

Fig. 6. Simulated single gamma ray response results with three incidence θ angles.

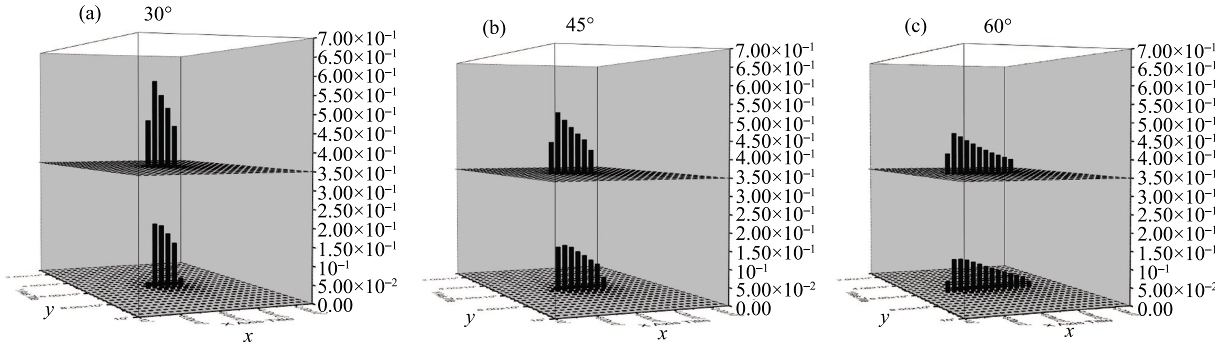

Fig. 7. Coincidence response function of TOR. The upper slice is calculated CRF and the lower slice is real CRF. x and y axes show relative element positions in detector coordinates.

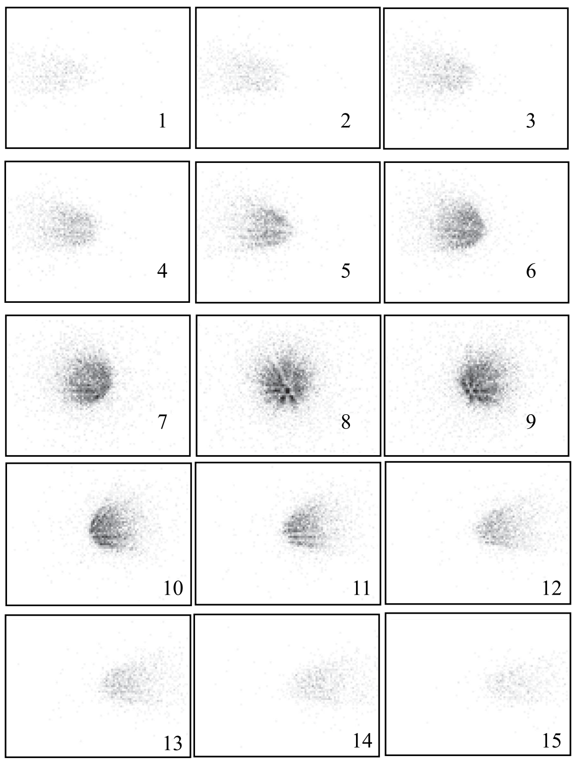

Fig. 8. Double-plane PET projection data representation.

2.3 PET implementation of the algorithm

To evaluate the algorithm, a PET system with two opposing detector heads was simulated. The distance between the two detector heads ranged from 1 cm to 6 cm, assuming this to be the distance range for breast imaging application. Both detectors contained 75 × 100 LYSO crystal elements. The crystal size was 1.9 mm × 1.9 mm × 10 mm, with a 0.1 mm gap filled with PVC. Note that the SGR simulated data were generated from the same crystal configuration as the opposing detector system, but with a proper crystal element number. Data acquisition and reconstruction were performed in 3D. The algorithm operation is described by matrix P in Equations (1–10). The matrix size of the reconstructed images in the in-plane was 400 × 300, with a pixel size of 0.5 mm. In the axial direction, the image pixel size was 1 mm. The image slice number was defined by the detector spacing, d. The geometric and blurring factors were both assessed, and the reconstruction was accelerated with OpenMP parallel programming support. The reconstruction using the blurring factor modeled system matrix was referred to as the RM reconstruction. To assess the impact of the geometric components on the image quality, a cube (16 pixels in side length) and a sphere (16 pixels in diameter) source with ^{18}F were placed in air. The two shapes both had an activity concentration of 5000 Bq/ml. Reconstructions without blurring factor were tested with three different geometric weights: the ray-driven model [20], the solid weight model [19], and the new tube area model, respectively. The sino data were reconstructed with EM (30 iterations, no subsets). All ranges of data in the sinogram were used.

A numerical micro-Derenzo phantom was used to generate noise-free data and to test the blurring factor. The diameters of the hot spots in the phantom were 2.4 mm, 2.0 mm, 1.7 mm, 1.35 mm, 1.0 mm, and 0.75 mm, respectively, and the center-to-center distance between the spots was twice the hot spot diameter. All the hot spots had an activity concentration of 5000 Bq/ml. The height of the phantom was 10 mm, with the axis vertical to the in-plane direction. The phantom was located at the center of the FOV. The distance between the two detector heads ranged from 1 cm to 6 cm, with the reconstructed image slices ranging from 10 to 60. Data were reconstructed by the 3D maximum likelihood estimation model, with (RM) or without (no-RM) the blurring information in the SRM. Only the true coincidence events were used. We chose the image reconstructed after 15 iterations and plotted the images in the center in-plane slice.

The noise properties were evaluated with a cylinder contrast phantom (cylinder length 10 mm, radius 27 mm). This phantom consisted of five hot spherical inserts of decreasing size, containing a uniform background activity concentration of 5000 Bq/ml. The embedded five hot spheres had a radius ranging from 1 mm to 5 mm, and all had a 4:1 ratio to background activity. The phantom was placed at the center of the FOV. The detector distance was 2 cm. Contrast recovery and noise characteristics were investigated and compared between the RM and no-RM algorithms. The contrast ratio was tested for each sphere i. The ratio value was calculated by the mean signal for each sphere S_i, against the background, B_i. Background volumes of interest (VOIs) of the same volume as the spheres were chosen between different in-planes at each sphere's (x,y) location.

The contrast ratios for each sphere were as follows:

$$\text{contrast ratio} = \frac{\langle S_i \rangle}{\langle B_i \rangle} \tag{14}$$

The background SN for each sphere was then found using:

$$\text{SN} = \frac{\text{std}\langle B_i \rangle}{\langle B_i \rangle} \tag{15}$$

where $\langle\ \rangle$ represents the mean and std( ) is the standard deviation across all pixels.

3 Results

3.1 Geometric component

Figure 9 shows the comparison results of the ray-driven model [20], the solid weight model [19], and the new tube area model, respectively. It shows that a dramatic improvement is obtained with the latter. A fairly smooth result was obtained with the tube area model, while artifact errors are shown in the other two models.

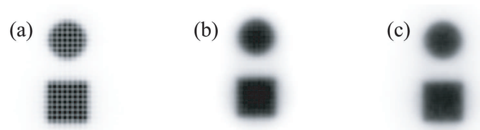

Fig. 9. Reconstructions of source data for different geometric models. (a) Ray-driven model (b) solid angle model (c) tube area model.

3.2 Blurring component

Figure 10 shows the reconstructed image of the micro-Derenzo phantom. The hot rods with a diameter of 1.35 mm are identified in both the RM and no-RM image data. In addition, the structure of the region containing 1.0 mm diameter rods are also observed in the data with RM data, while hot rods of the same size are blurred in the no-RM data. The RM data show an improved visual recovery of the smallest spheres, and better delineation of the structures in the RM reconstructed images are observed. The no-RM data show an increased blurring effect as the detector distance becomes smaller. The results show the profiles of the third line hot spots in the micro-Derenzo phantom. Overall, the contrast of the hot rods against the background remained identical in RM and no-RM. The graph of the selected three group hot rods show that slimmer profiles were observed when RM was used, leading to lower spatial variance. All the images are shown with the same viewing window width, but slightly different viewing means.

3.3 Quality study

Figure 11 show the impact of the RM on reconstruction of the noise properties. The contrast ratio plot show that the background contrast was improved with RM data for each sphere size. However, the background noise ratio was decreased with each VOI for all sizes of sphere. It was confirmed that RM significantly reduced the voxel variance to a level comparable with the level that was obtained after reconstruction without RM. Figure 11 demonstrates that higher positive correlations with adjacent voxels were observed when RM was used, leading to lower spatial variance.

3.4 Computation burden

Table 1 shows the reconstruction parameters of the system. Although the double-plane system is compact and small, there is still a 1.35×10^{14} (the image matrix size $\times$ the sinogram matrix size) computation burden. The reconstruction time performance was tested with different span data. The sinogram data were reconstructed with all, 1/2, 1/4 and 1/8 span respectively, to test the computation burden. Computation times with one iteration are listed as follows, as well as the image results after one iteration (see Table 2 and Fig. 12).

Table 1. Parameters of reconstruction method.

parameters	values
image space/cm	20×15×2
voxel size/mm	0.5×0.5×1.0
image size	400×300×20
crystal number/detector	100×75
crystal size/mm	1.9×1.9×10
sinogram size with all span	100× 75×100×75

Table 2. Reconstruction time.

span	coincident event($\times10^4$)	no-RM recon time/min	RM recon time/min
8/8	606	21.23	86.23
4/8	473	9.53	40.62
2/8	191	2.86	11.98
1/8	58	0.75	1.63

Figure 12 shows that the RM reconstruction gives image recovery with more data information, as well as prolonged time consumption. With all the span data, the RM method took more than 86 minutes to perform one iteration.

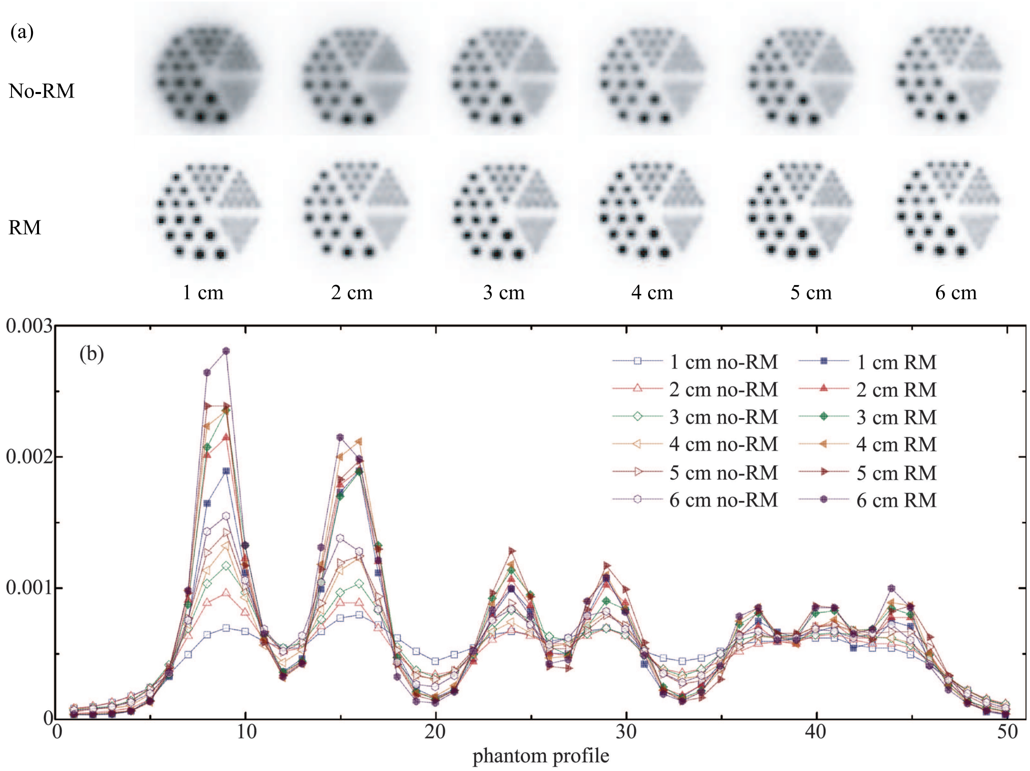

Fig. 10. (color online) Micro-Derenzo phantom results.

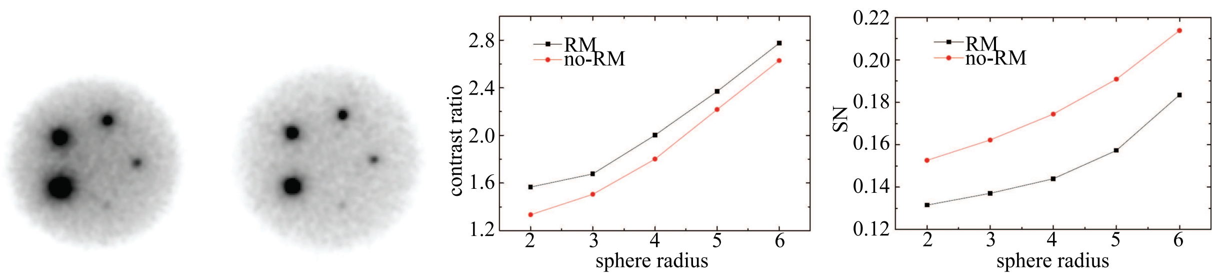

Fig. 11. (color online) Quality phantom results.

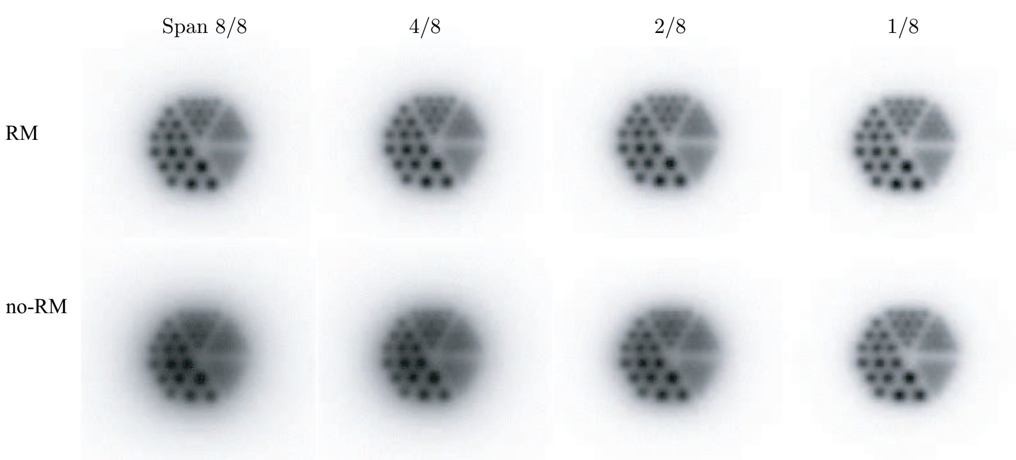

Fig. 12. Quality phantom results.

4 Discussion

The results show that RM in the reconstruction process improved spatial resolution (giving improved delineation of the structures), improved contrast recovery, and also improved the noise properties of the images. The method has the following features: (1) it is applicable for different plane distances; (2) it is efficient in simulation; (3) it is effective for resolution recovery; and (4) it is robust in noise suppression.

When employing double-plane geometry, the artifacts that result from missing data mean that the existing analytic reconstruction methods will not work well. In contrast, based on a statistical model, iterative reconstruction algorithms are capable of maximizing resolution recovery by accurate modeling of the system response. Furthermore, iterative reconstruction methods can optimize performance in low-count situations. Therefore, an iterative method was applied in the present study. The accurate system modeling was focused on geometric and blurring components.

It is interesting to note that the artifacts in Fig. 9(a) and (b) are grids shaped in both x and y axial directions. The errors were probably generated as a result of the discontinuous “square pixel” modeling of the reconstructed image. The discrete contribution could be compensated in a full ring detector with oversampling data. However, the effect cannot be ignored in the plane system while the data are missing in the sampling transection. Based on the intersection area between voxel and tube, the algorithm provides superior accuracy and smooth geometric sensitivity weights without loss of resolution. Furthermore, the tube area model has the advantages of the parallel attributes of the image space, and is applicable for the double PET system.

The blurring component was based on a single gamma response calculated model. The simulated single gamma response matrix size is a trade-off between precision and computation burden. We took 33×33 crystals in SGR simulation because the blurred TOR number is a 4^{th} power of the simulated crystals. That means for each incident TOR, 33^4 blurred TORs should be calculated. (The corresponding computation burden will be discussed later in the limitations). When the incidence angle is extremely oblique, precision for the tail-cut is lost because of the limited simulated crystal array. However, the precision lost is less obvious in the reconstructed result, as shown in the micro-Derenzo phantom and quality phantom. In addition, a simulated matrix reduction to obtain a fast computation rate is currently in further study.

Operating as in traditional mammography, the system could result in substantial parallax errors. When the distance between the double-planes becomes smaller, the TOR is more likely to encounter an oblique angle. Reconstructed images with 1 cm spacing showed severe blurring effects that were relieved when the plane distance became large. In a ring PET detector, to obtain images with an acceptable level of resolution uniformity, most systems restrict their FOV to 1/2–2/3 of the detector ring size. Nevertheless, in the double-plane system, the reconstructed results of the micro-Derenzo phantom demonstrated that the blurring effects could be well compensated for, even with a plane distance of 1 cm. Therefore, the system configuration could make use of more span data and achieve a shorter scanning time without loss of resolution.

The reconstruction time is the limitation of this method. With a changeable distance between the planes, the problem is more complicated, since the system response matrix should be calculated in real time. As the time performance showed, the RM method took more than 86 minutes to complete one iteration for all the span data. Although the blurring effect were well recovered, the method is still not applicable for the computation burden reason. Therefore a graphics processing unit (GPU) acceleration method would be expected.

There is another limitation that should be seriously taken into consideration: the gaps between the blocks in the real system are not constant, but the system simulation and the CRF simulation were both based on the assumption that gaps between crystals were all the same. How this simplification would affect a real system should be further tested with hardware. That means the block edge effect is ignored. The positron range effect is negligible with ^{18}F tracers, but should be considered for a new radiotracer with a larger positron range.

5 Conclusions

A high resolution reconstruction method for a double-plane PET system was studied for breast imaging. The plane spacing is supposed to be changeable. A finite geometric sensitivity model was applied, and an RM derived from a single gamma response was studied. In addition, resulting improvements in contrast recovery of small structure and noise properties in images were demonstrated. This approach makes a high spatial resolution reconstruction method available for differently sized breast imaging applications.

References

1 M. C. Abreu, et al, Nuclear Science, IEEE Transactions on, **53**(1): 71-77 (2006)
2 S. L. Bowen, et al, Journal of Nuclear Medicine, **50**(9): 1401-1408 (2009)
3 M. Furuta, et al, Basic evaluation of a C-shaped breast PET scanner, *Of the 2009 Nuclear Science Symposium and Medical Imaging Conference Record* (NSS/MIC), 2009
4 P. Lecoq, and J. Varela, Nuclear Instruments and Methods in Physics Research Section A: Accelerators, Spectrometers, Detectors and Associated Equipment, **486**(1): 1-6 (2002)
5 L. MacDonald, et al, Journal of Nuclear Medicine, **50**(10): 1666-1675 (2009)
6 R. R. Raylman, et al, Physics in Medicine and Biology, **53**(3): 637 (2008)
7 C. Thompson, et al, Medical physics, **21**(4), 529-538 (1994)
8 B. Koolen, et al, *Molecular Imaging in Breast Cancer: from whole-body PET/CT to dedicated breast PET,* Journal of oncology, 2012
9 R. R. Raylman et al, Journal of medical imaging and radiation oncology, **55**(1): 58-64 (2011)
10 M. Iima, et al, Journal of Nuclear Medicine, **53**(10): 1534-1542 (2012)
11 J. S. Eo et al, The Breast, **21**(1), 66-71 (2012)
12 C. M. Kao, Y. Dong and Q. Xie, Evaluation of 3D image reconstruction methods for a dual-head small-animal PET scanner, *Of the 2007 Nuclear Science Symposium and Medical Imaging Conference Record (NSS/MIC),* 2007
13 A. Saoudi, et al, Nuclear Science, IEEE Transactions on, **46**(3): 462-467 (1999)
14 J. Seidel et al, Nuclear Science, IEEE Transactions on, **46**(3): 485-490 (1999)
15 W. Moses, and S.E. Derenzo, Nuclear Science, IEEE Transactions on, **41**(4): 1441-1445 (1994)
16 G. Boning, et al, Implementation of Monte Carlo Coincident Functions in Image Generation of a High Resolution Animal Positron Tomograph, *Of the 2000 Nuclear Science Symposium and Medical Imaging Conference Record (NSS/MIC),* (2000)
17 C. M. Kao, and C. T. Chen, Nuclear Science, IEEE Transactions on, **49**(1): 208-214 (2002)
18 V. Y. Panin, et al, Medical Imaging, IEEE Transactions on, **25**(7): 907-921 (2006)
19 J. Qi et al, Physics in Medicine and Biology, **43**(4): 1001. (1998)
20 P. M. Joseph, Medical Imaging, IEEE Transactions on, **1**(3), 192-196 (1982)
21 A. Terstegge, et al. High resolution and better quantification by tube of response modelling in 3D PET reconstruction, *Of the 1996 Nuclear Science Symposium and Medical Imaging Conference Record (NSS/MIC),* (1996)
22 C. Johnson, et al, Nuclear Science, IEEE Transactions on, **42**(4): 1223-1227 (1995)
23 C. Chen, S. Y. Lee and Z. Cho, Medical Imaging, IEEE Transactions on, **10**(4): 513-522 (1991)
24 A. Rahmim, J. Qi and V. Sossi, Medical physics, **40**(6): 064301 (2013)
25 V. Y. Panin, et al, PET reconstruction with system matrix derived from point source measurements, *Of the 2004 Nuclear Science Symposium and Medical Imaging Conference Record (NSS/MIC),* 2004
26 F. C. Sureau et al, Journal of Nuclear Medicine, **49**(6): 1000-1008 (2008)
27 X. Y. Gu et al, Chinese Physics C, **10**(22): 108-202 (2015)
28 R. M. Leahy, and J. Qi, Statistics and Computing, **10**(2): 147-165 (2000)
29 F. Xin et al, Chinese Physics B, **24**(1): 018702 (2015)
30 S. R. Cherry, and M. Dahlbom, in *PET: Physics, Instrumation, and Scanners*, ed. M. E. Phelps, (Springer, 2006)